An Opposed Jet, Process Flow Geometry: Three-Dimensional Experimental Results and Simulation for Verification

Robert S. Brodkey[*], Matt Nilsen[1], Abdullahi Yusuf[1], Alex Brown[1], Miguel Garcia[1], Anita Kiprovska[1], James Knight[1], Elizabeth Lynch[1], Thomas Yang[1], Yang Zhao[1], and Shoichiro Nakamura[2]

[1] The William G. Lowrie Department of Chemical and Biomolecular Engineering, The Ohio State University, 140 W. 19th Ave., Columbus, OH 43210.

[2] Department of Mechanical Engineering, The Ohio State University, 201 W. 19th Ave., Columbus, OH 43210.

[*] Email: Brodkey.1@osu.edu
Phone: 614-292-2609
Fax: 614-292-3769

ABSTRACT

Experiments and computations were made using an opposed jet mixer. The experiments provided time-resolved, fully 3-dimensional velocity vector data of low resolution. Initial velocities for the computation were all zero. The computational inlet profiles were a parabolic distribution for laminar flow, 1/7th power law for the turbulent profile, or plug flow. Two time zones were observed: the first from the start-up jet flow to fully turbulent conditions and the second, the fully turbulent (pseudo-steady-state) conditions. The initial part (available for the computations) had the most interesting fluid dynamics. The laminar inlet is different than the others. The fully turbulent flow was further divided into primary or jets, secondary or pancake, and tertiary regions of low velocity. The long times needed to obtain an average in interacting jet flows are caused by low frequency flapping of the jets. The final comparisons between experiments and computations were within a factor of two.

Keywords: Transitional and Turbulent Flow, Particle Tracking Velocimetry (PTV), DNS and LES Numerical Simulation, and Validation of Experimental Results.

1. Introduction

This paper is a summary of work accomplished over the last 15 to 20 years. Our original study was to add to the understanding of the enhancement of mixing in dynamic systems; i.e., where there would be a superimposed oscillation added to the mean motion in a reactor geometry. A joint NSF grant supported the work where we used the opposed jet geometry for the turbulence study. At

Rutgers, Fernando Muzzio worked on laminar systems and at OSU, Bob Brodkey studied the turbulent counterpart. We later realized that for turbulent flows the full field and time resolved experimental data could also be used for testing computer fluid dynamics (CFD) methods. The same geometry and conditions were then used to obtain parallel computations for validation tests. There are, of course, many earlier validation studies in the literature, but nothing that would try to treat the time-resolved, velocity-vector field for the turbulence problem.

Our goal is to model mixing so that computations can be used to eliminate experiments. Our view must be well based in fundamentals, but be directed to solving real-world problems. To contribute to the solution, our attention is focused on the opposed jet system, which is simplistic, but of industrial importance. We view this system as key to the validation of computational results.

2. Experimental Analysis

2.1. Experimental Results

The experiments, when compared to the computations, are of low resolution. As a result, in the *time domain*, we did not have success in comparing computations and experiments because of the 100 fold difference in resolution and an inability to satisfy continuity when an experimental initial time condition is used to start the computations. The net result is that the experimental and computational comparisons had to be done for averages under *pseudo steady-state turbulent conditions*.

For each particle, a validated velocity vector is established. Then these are tracked frame to frame to establish the velocity vectors as a function of time. Each velocity value is based on pairs of video images taken at right angles at a rate of 30 fps. The entire flow field is viewed in each image. Planar lighting is not used as is done in laser Doppler methods. Thus, the particle density used must be low enough so that stereo pairs of individual particles can be established. As a result, each frame had on the order of a thousand particles in view. The final vectors count on each frame was usually less than 700 vectors. The key background references are by Guezennec and Brodkey *et al.* 1992 to 1998.

Our unique experimental measurements have modest resolution, but the results are full-field and time-resolved. The geometry of the opposed jet system is shown later in Fig. 6, where the computational grid is also shown. To help the reader grasp a feel for the magnitude of the task, 18 independent image sets were obtained with each having at least 2,000 images each (> 66.67 sec). In all, there are over 20 minutes of real time data. The total frames (> 36,000) should be adequate for a

reliable statistical average that generated 12,938,071 vectors. The resolution selected for presentation of the experiments was 21 slices in each of the three directions. Thus, in the experiments there are 21^3 = 9261 nodes reported. Clearly the resolution is low when compared to computational results (1:100). The analysis program does a spatial average rather than a time average across many frames as was done in CFD computations. However, the unique net result was a reasonably low-cost system that could provide three-dimensionally resolved velocity vector data in time.

A great deal of additional work was needed to understand and establish the reliability of both the experimental and computational efforts and the analysis of the results. For example, for the experiments, we had to introduce a geometric limit as the x,y,z system used in the experiments can be outside of the r,θ,z system used in the computations. If these were used it would introduce many zeros in the averaging. Thus, we put a limit on the root of $r^2=x^2+y^2$, which must be less than the CFD r used [note: only the polar or horizontal plane (x, y) is used for this]. We also used different sub-regions of the flow to help in the analysis. The sub-regions were often a small region centered on the impingement location of the two jets or sub-regions of the jet itself. For details of the flow in the fully developed turbulent region, one of the four symmetrical quadrants of the container volume (again see Fig. 6) and its sub-regions were used.

One would normally think that for the long time average, the flow would be symmetric; however, this depends on what is meant by a long time average. For contained flows, such as in a pipe, the needed averaging time is small. For a flapping jet, the needed time is longer because of low frequency (long time) flapping. Thus, we need to check longer than normal averaging times. Often in the literature, only the average and RMS are used to provide validation checks. However, we also report the skewness and kurtosis, as these higher order moments are more sensitive to having adequate statistical samples.

The qualitative aspect of our study was to visually look at the resulting vector and contour representations of the flow field for both the experimental and computational efforts and to compare them. Since the experiments are restricted to the fully turbulent region, any comparison between the two must be done in that region. Again, the statistical averages of the first four moments were used. These were determined, as well as possible, from the experimental data by using about the same regions of the flow field as used for the computational results. The long-time average study can provide a measure of the overall ability of the code to reproduce the experimental results.

There are a multitude of steps needed to accomplish quantitative results all of which must be programed to automate the analysis. The remainder of this section addresses most of these items. Human stereoscopic viewing is not adequate. The small angle between our eyes makes the accuracy of measurement in the direction away from the lens inadequate. Thus, orthogonal picture pairs of images were used. With this, the vertical velocity is redundant between the two images. What now becomes the major task in multi-particle tracking is the establishment of the same particle in both views and the computation of that particle's velocity.

To obtain quantitative data, the system must first be calibrated. This is a major task in itself. The use of ray-tracing techniques is time consuming with all the surfaces at which the index of refraction changes; thus, this approach was rejected. Rather, a small pin-point of light placed at many known 3-D positions in the flow by a mechanical mechanism and a corresponding code was used to determine the actual x & y locations in the resulting pair of images. The known 3-D locations and the positions in the two images were used to establish a set of optimized equations for calibration. For additional information see Kent *et al.* (1993) and Guezennec and Choi (1997).

From pairs of images from any given experiment, the next task is to establish, automatically, the particle pairs. This is easy when only a few particles are in view at a time, but impossible when one wishes to track in 3-D on the order of a 1000 particles at the same time. Rather, the approach used was to track the particles in each camera image separately using a sequence of five images in time to establish particle paths. The computer steps involved image enhancement by background removal, generating binary images, matching, etc. There are many criteria that were used for the matching evaluation to be sure that only matched paths were obtained. For example, one key criterion dictated that particle pairs must both be located at the same z - position (vertical). When the paths had been established, they were matched in space to establish the final 3-D path. The physical location of all the particles in the 3rd frame (middle one) was then determined and the velocity for each one established from a 5-point sloping formula. It is important that only true velocities be determined. Thus, the multiple criteria that were used reduce the available vectors from maybe a 1000 to 700 or less per frame; but, it is better to provide more input data than to dilute real velocity values with false values. To proceed, the first frame in the sequence of 5 was then discarded and the next frame added to the end. The old 4th point has now become the new 3rd point. The tracking technique then started

anew, which avoided accumulating errors. All of these steps were fully automated to operate on the PC's available.

In any given pair of images used to establish the particle positions, the particle locations were random. Thus, once all the vectors were available, the vector field was established using 21^3 = 9,261 nodes. This was accomplished by an interpolation-extrapolation technique. Each of the images set was independent of the other sets as there was on the order of 10 minutes between sets. However, any one of them provides a time-resolved picture of the flow for the minute or so of run time.

As noted previously, the qualitative aspect of our study was to look at the resulting vector and contour representations of the flow from both the computational and experimental efforts and to compare them. Our quantitative measurements are the statistical averages of the first four moments. These were determined, as well as possible, from the experimental data using about the same region of the flow field. This long-time average study can provide a measure of the overall ability of the code to reproduce the experimental results.

In addition to the long time average flow pictures and moments, the nature of the flow can be observed by using dynamic sequences. However, a detailed numerical analysis of the experiments in the time domain adds complications. Any one frame does not have enough vectors (~ 700) to give a statistical representation of the instantaneous three-dimensional flow field. Thus, a number of frames (we settled on using 11) had to be averaged to provide enough vectors for this purpose. This is an additional time window smoothing filter of the data to obtain what would be a smooth picture of the flow field. For example, for the 11 point window, the average would represent point 6, the midpoint. Just as was done in the tracking, the next point (7) would be obtained by eliminating the first frame of the 11 and adding the next new frame (12), still resulting in a total of 11 frames. The average would be repeated to establish the picture at the time corresponding to frame 7. The moving window average technique provides enough vectors per frame so that the visuals are reasonably smooth. A few frames are, of course, lost at the beginning and end of a sequence as a result of the technique. For the computations, this is not a problem since the time steps and the special grid are very small.

2.2. Results for Averaging Time for the Experimental Data

To determine the time needed to obtain an average in the fully turbulent region, accumulative plots were used. Each point on any curve is the accumulation of all of the data from the start of the fully turbulent conditions (start of curve) to the time for that specific point. The lines end at 235

seconds of accumulated time. The following example (Fig. 1) for the experimental values of the RMS is better seen in the online color figures. The other moment figures (average, skewness, and kurtosis) and further comments can be found in the supplemental material online (SMO_01_Experimental Averaging Time). The file SMO_00_Fig Info Chart is a summary of all the dynamic visuals that are linked to OSU's Knowledge Bank. In general, the supplemental material involves the three-dimensionality of the flow, higher-order statistical moments, further statistical measures, comparisons between experiments and computations, and time dependency aspects of the research. The experimental moment plots differ in detail, but they are all superficially similar. The averaging shown was matched as well as possible to the same symmetric sub-area as for the computations, which was the central core area. The *x*-axis is the number of vectors represented. Because of the large sub-volume, later comparisons between the computational and experimental plots are qualitative in nature. The error bars are at 1% and are only shown on the x velocity for clarity.

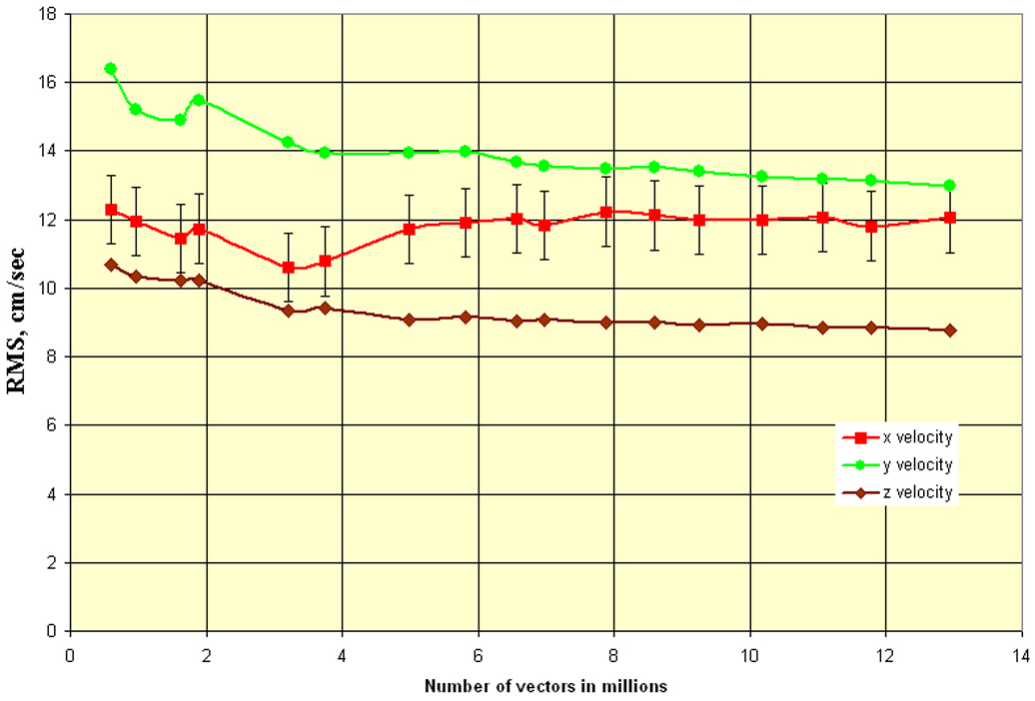

Fig. 1. (see Color version online). Accumulative Experimental RMS, cm/sec

It takes about 5 million vectors to arrive at a reasonable average velocity. The RMS requires more vectors (~ 7 million) than the average. The skewness requires on the order of 10 million vectors and for the kurtosis, 7 million. We have not shown the error bars in the higher moment plots since these moments are small and even the 1% error levels are very large.

2.3. Visualization of the Experimental Results

The coordinates used in the experimental work were rectangular while those for the computations were cylindrical. More details about the coordinate systems used are presented in the supplemental material online (SMO_02_Coordinate Systems for the Experiments and Computations). To be sure we are viewing the same thing in both data sets, we compared the 3-dimensional figures for the computations and the experiments. Figure 2 is a qualitative comparison of the long-time average for the fully turbulent conditions. The two pictures have been oriented and scaled so that they would be about the same view. The experimental jets look broader than the computed values. We suspect that in the experiments, the inlet conditions were not the desired idealized parabolic laminar flow all the time (maybe transitional or even turbulent at times). As a result, the jet wandered more in the experiments than in the computations. The experimental inlet pipe Reynolds number was set at 2000. The possibility of transitional or turbulent inlet jets led us to do additional CFD runs to be discussed later with inlet profiles as turbulent or plug flow.

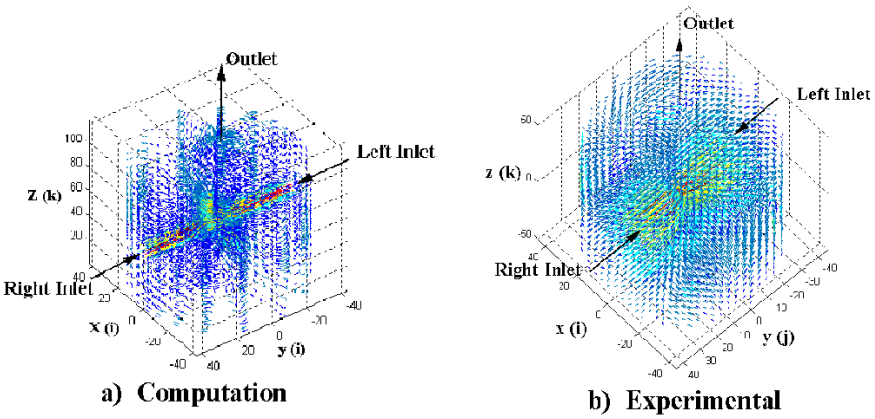

Fig. 2. (Color online). CFD velocity vectors on left (a) plotted to match the experiments (b).

In the preceding visual, the 3-D presentation is too complex for details to be extracted. Two alternate 3-D representations can help in our understanding. These dynamic visuals must be viewed online. In Fig. 3 on the left, we start with the highest velocity level and replace each level of velocity with the next lower level. Thus, the visual starts with the highest level and ends with the lowest. The velocity level is shown by the color bar to the right and along the bar a moving arrow indicates the velocity level. In the right view, rather than replacing each level with the next lower level, the velocity level is added. Thus, the visual starts with the highest level and ends with the entire 3-D flow.

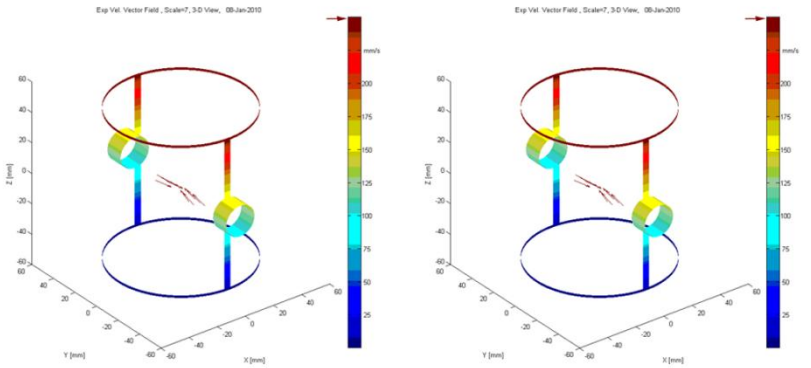

Fig. 3. (Link to Dynamics and Color in 'ppt' format). *Left*, each level of velocity is replaced with the next lower velocity level. *Right*, rather than replacing each level with the next lower, it is added. The left visual starts with the highest level and ends with the lowest. The right visual also starts with the highest and ends with the full vector field. The velocity level is shown by the color bar to the right and along the bar a moving arrow indicates the level. The dynamic figure then repeats.

Figure 4 is the horizontal plane or top view (*xy*) scanned from top to bottom and then the scan repeats. This is one of three views that provide dynamic scans of the experimental results for the three coordinate directions. An arrow (red online) shows the position of the plane being viewed. The other two views are discussed and presented in the supplemental material online (SMO_03_Two dimensional scans across the flow). Because they are dynamic visuals they have to be further linked

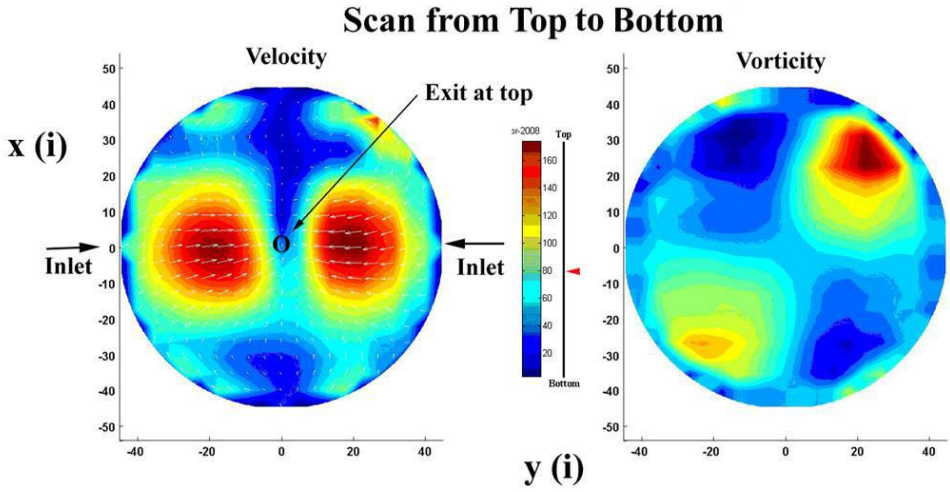

Fig. 4. (Link to Dynamics and Color in 'ppt' format). Top (*xy*) view of the flow in horizontal planes. The arrow (red online) in the center indicates the position of the plane being viewed. The left view is contours of the *velocity vector* field. Also, because of the reversal in sign in the code for the radial (*r* or *x*) velocity, the colors in the view on the right for the *derived vorticity* are reversed (i.e., here light or blue is '+' and dark or red is '-').

to OSU's Knowledge Bank. These views are the front vertical view (yz) in the planes that are scanned from front to back and the cross or orthogonal vertical view (xz) that is scanned from left to right.

There are several additional points to note: in all of the three directions there is not enough data to plot contours for the very top and bottom levels (1st and 21st). For the horizontal scan, the top is actually the 20th plane (rather than the 21st). Also, in Fig. 4 there is an "**O**" in the center that shows the specific horizontal location of the exit jet. All the flow leaves at the top and there is no flow out the bottom.

As noted in the title of Fig. 4, the derived vorticities shown are colored opposite the conventional usage of red for + vorticity and blue for - vorticity. Thus, the results are as expected and represent, on the average, counter rotating vortices in the central region. The most important observation is that the resolution is low so that one cannot verify that the inlet flows for the experiments are laminar, transitional, or turbulent on the average.

Since the 3-D view in Fig. 2 is not clear because of the complexity, we modified the figure further to show limited regions of the experimental and CFD results (CFD on the left from Fig. 11). These are the most dramatic regions of the flow and are shown in Fig. 5. The size of the right image is smaller as measurements were only made over the region marked by the pair of superimposed rectangles on the left figure. The lower resolution and the more diffused picture of the flow in the experiments are obvious. However, in spite of the duality of the coordinate systems used, it is clear that we did have the experimental and computational results properly oriented.

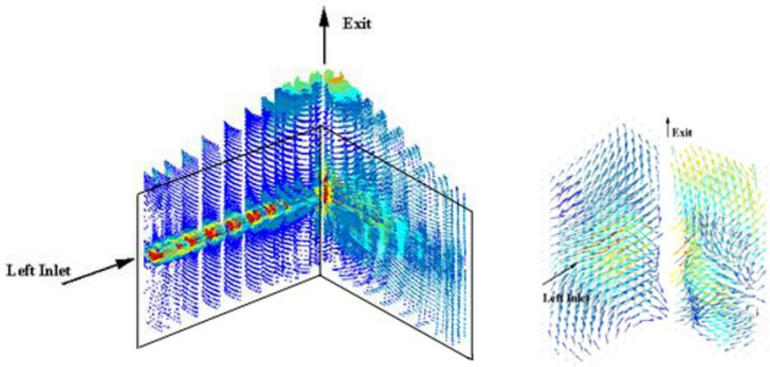

Fig. 5. (Color online). Left, CFD simulation and right, experiments.

It should be emphasized that the averages shown in these figures are from an average of nearly 13 million measured vectors. These averages are made up of 18 individual time sequences. The possibilities of utilizing time sequences will be discussed later. However, we know of no other measurements like these that have been done.

For the experimental effort, still other important points can be found in the literature references (Guezennec and Brodkey *et al.* 1992 to 1998). Some additional experimental areas covered are lighting, framing rate, images required, and the difficulty of using ray-tracing techniques. For the data analysis, some areas are particle tracking, sloping techniques to establish velocities, establishing a fixed grid from a field a random velocities, and averaging methods.

3. Introduction to Numerics

Three ways of simulating the flows in chemical mixers and reactors can be used: 1) direct numerical simulation (DNS), 2) large eddy simulation (LES), and 3) Reynolds-averaged Navier-Stokes (RANS) equations. DNS is used to solve the Navier-Stokes equations without modeling the turbulence and is applicable for all flow regimes. LES models only the smallest turbulent scales that are below the resolution of the computational grid. RANS is used for engineering purposes since it is the least computational burdening. This paper addressed the DNS and LES steps in our attempt to validate time-resolved, three-dimensional velocity vector data.

The initial conditions at t=0 for the velocity were all set to zero and thus the computations included the start-up jet flow. The flows developed as a result of the fixed inlet conditions of laminar, turbulent, or plug flow. All wall velocities were set to zero. Given enough averaging time, the fully turbulent results should be independent of the inlet jet conditions. Figure 6 shows the system geometry and grid. There are additional questions that must be addressed to insure that the numerical results are reasonably correct so that comparisons can be made to experiments. How insensitive are

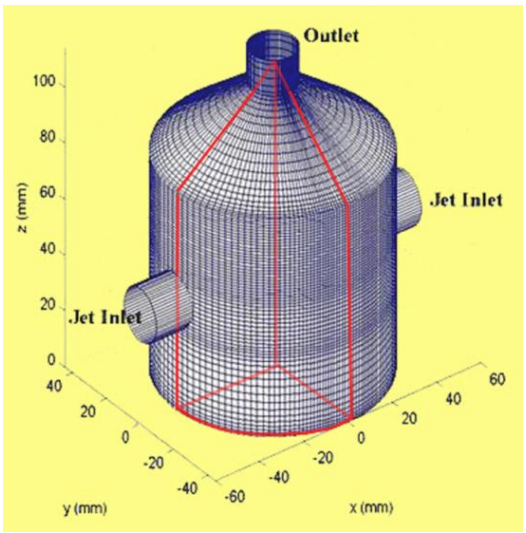

Fig. 6. (Color online). The opposed jet geometry and grid used for the computational analysis. The outlet was extended to match the experiments. This figure is for the reference grid run. The outlined quadrant (red) is the main test volume (called left front, SV#15) used for the evaluation of the statistics.

the results to a decrease in the time step used in the computations. What averaging time is adequate so that statistical representative measurements can be obtained? And what level of grid resolution has been achieved? These questions and more have been addressed with the results being reported in the supplemental material online (SMO_04_Additional Numeric Details).

For the simulation, the code solves the three-dimensional unsteady incompressible Navier-Stokes equations by the finite difference approximations in a strong conservation form on a structured grid. The convection terms were discretized by the central difference approximations and added with the fourth-order numerical viscosity terms. To decrease the chance of spurious oscillation due to the point-centered grid, the Rhie-Chow interpolation scheme was adopted. The basic information of the solution algorithms is available (Nakamura and Brodkey *et al.* 1982 to 2002). Some additional, brief comments can be found in the supplemental material online (SMO_12_The computational effort).

The DNS grid was the largest that could be used with the FORTRAN code available. The LES approach normally uses a lower grid density than used for DNS to speed up the computation and then model the sub-grid level to improve the representation of the turbulence. The LES approach used here was to use the same grid as used in the DNS and improve the simulation by adding sub-grid modeling. Thus, the LES uses an identical grid to the DNS and only adds a sub-grid eddy viscosity term. Our view of the DNS approach is that the resolution needed for numerical stability is a trade-off for sub-grid smoothing that is used in the LES approach. We would like to have better resolution for the DNS work, but that was not possible. The similarity of the jet development between the two computations suggests to us that the effort was worthwhile and some comments are presented in the paper and the supplemental material online. However, only the LES results are reported.

The inlet jets were set as boundary conditions: an inlet parabolic velocity distribution as expected for laminar flow, a $1/7^{th}$ power law for an average turbulent profile inlet, and plug flow. The inlet jets provide the driving force for the flow.

For analysis, the computations were divided into two time zones. The initial zone was from zero until we judged that fully turbulent conditions were established. The initial time period had the most interesting fluid dynamics. The second time zone was a much longer period to establish fully turbulent flow for determination of the statistical moments through the kurtosis. The long times needed for averaging when compared to pipe flow are caused by low frequency flapping of the jets.

Our first observation is that under fully turbulent conditions, DNS and LES are two different instantaneous realizations of the flow. Thus, the two realizations have to be compared using long-time-averages. However, we did gain some insight by looking at the initial developing jets resulting from using the two computational approaches. There is an important proviso that must be injected here when looking at the initial period. We must ask are the instabilities (or lack thereof) observed as a result of fluid or numerical perturbations? Showing detailed time sequences here are visual overload and not our main goal. Thus, we will describe in words the differences observed and the implications derived.

For the LES results, all three jet inlets cases ran well into the fully turbulent region until stopped by our having accumulated enough data. However, both the laminar and turbulent inlets using DNS failed just before the two jets arrived at the stagnation point (i.e., where the two jets pancake). This must be a result of numerical instability because when viewed, the computations are clearly not realistic. The DNS solution for plug flow ran like the LES version and the long-time averages are essentially the same. Because this involves comparisons between computed results and because we feel that using the sub-grid eddy viscosity approximation (LES) as an extension of DNS is a sound idea, only results computed by the LES sub-grid model are presented in detail in this paper.

The side by side visual comparison was carried out to over 25 seconds of real time, when both versions were well into the fully turbulent region. There are only small minor differences between the DNS and LES computations up to the time (< 4 sec or 7000 time steps) when the jets create a stagnation point and the resulting pancake spreads towards the wall. For the next 10 to 15 seconds (of the order of 20,000 time steps) each flow maintains a degree of symmetry between the left and right jet sides. There is a sense of overall similarity between the DNS and LES cases through this entire period, but not in the fine detail. The stagnation point of the two high-speed jets is a source of low-speed turbulence that moves outward from the stagnation point to fill the bulk of the volume. The DNS at first spreads faster than the LES version, but on reviewing several more times it appears it is just an alternate path to the fully turbulent conditions, which are realized for both cases at about 30,000 time steps (~ 17 sec).

Once last comment on the source of the instability: physical or numerical. The three LES simulations (different inlets) all ran properly and can be interpreted nicely in terms of shear-layer instability. The numerical failure on the DNS laminar inlet case must be a result of the lack of resolution or the small eddy dampening at the sub-grid level. There is no physical explanation that can suggest why, with eddy viscosity, the laminar jet case is clean and the ultimate break down proceeds via a recirculation pattern. Without eddy viscosity the

computation shows similar pulsing as for the other two inlets and fails because of pressure imbalance. To add to this, why would the turbulent inlet under DNS conditions fail (no eddy viscosity) and the plug inlet run under both?

3.1. General Comments

To start the numerical analysis, conditions were selected from the past experience of the author of the DNS/LES code (SN) that suggested to him what would be adequate. A series of runs were then made to test time step sensitivity, vertical resolution, and inlet flow conditions. We used ten seconds of real time data in the fully turbulent region for the time-step comparison. These comparisons were made over a limited central core region (SV#21: a circular disk shaped volume, also see section 4.1) that contained the opposing jets. We halved the time step, which made little difference (~ 2% or less, except for the kurtosis ~ 5%). These percentage differences are reasonable given the small sample used. Certainly, had we used a longer time-segment of data, the results would have been closer.

Every 60th time step was retained to well over 400,000 steps, which is over a real time of 225 seconds. The computer outputs were stored (every 0.0338 sec). The experimental video data acquisition rate was 30 fps (every 0.0333 sec), which is close to the same rate. The comparison of the statistics was made at four moment levels: average, RMS, skewness, and kurtosis or flatness. For these comparisons, the vessel (Fig. 6) was split into 4 quadrants, which are geometrically symmetric (see supplemental material online, SMO_06_Quadrant Analysis). We arbitrarily selected the left-front one for our detailed analysis. We did compare the other three quadrants in more detail and found little difference on the average for these.

An increase in the vertical resolution of ~ 43% was used in the local region used for testing. The last 144,000 time steps (~ 160 seconds of real time) were used for the comparison. The average changed by 25-30%, the RMS by 10-25%, and the skewness and kurtosis by 20-45%. This is certainly higher than we would like, but is the best we could do at the time using PC's as our computer base. It should again be noted that the experimental grid size is 2 orders of magnitude cruder.

Comparisons of the LES and DNS results could only be done for the plug flow case where both the DNS and LES computations were available. The results are very nearly identical; thus, additional visuals are not presented. The grid was the same in both and the only difference is that the LES run had a sub-grid eddy viscosity term for modeling. For the plug flow inlet using LES, the *r*-component in the left jet sub-volume was 7.64 cm/sec, which varied only 1.2% from the DNS value. These are

not expected to be exactly the same because we really have two different realizations in the fully turbulent region. Because the θ and z velocity components are small, percentage differences based on component velocity can be large. Using the r-velocity as our reference for comparison resulted in 4.9% and 1.1% differences, respectively.

For the entire quadrant, the average r-component velocities are an order of magnitude smaller than in the jet because of the existence of both positive and negative values around zero. The velocities are even smaller for the θ and z components. However, using the r-velocity component in the jet as our basis for comparison, the difference in the average velocities was about ± 10%.

3.2. Sequences of the Instantaneous Flow Field for Different Inlet Conditions

Two dynamic visual examples are used here to illustrate how we presented the results for visualization of the flow. For the most part, our analysis was based on the laminar input case which used the enhanced vertical grid and improved entry conditions. To evaluate these results in more detail, instantaneous videos and averaged pictures of the flow field were generated using horizontal and vertical planes at the midpoint of the volume. These visuals are dynamic 'gif' files imbedded in an 'htm' format that is relatively small, but still, take time to download (< 5 min for the largest). Both velocity vector fields (Fig. 7) and velocity magnitude contour plots (Fig. 8) were used to

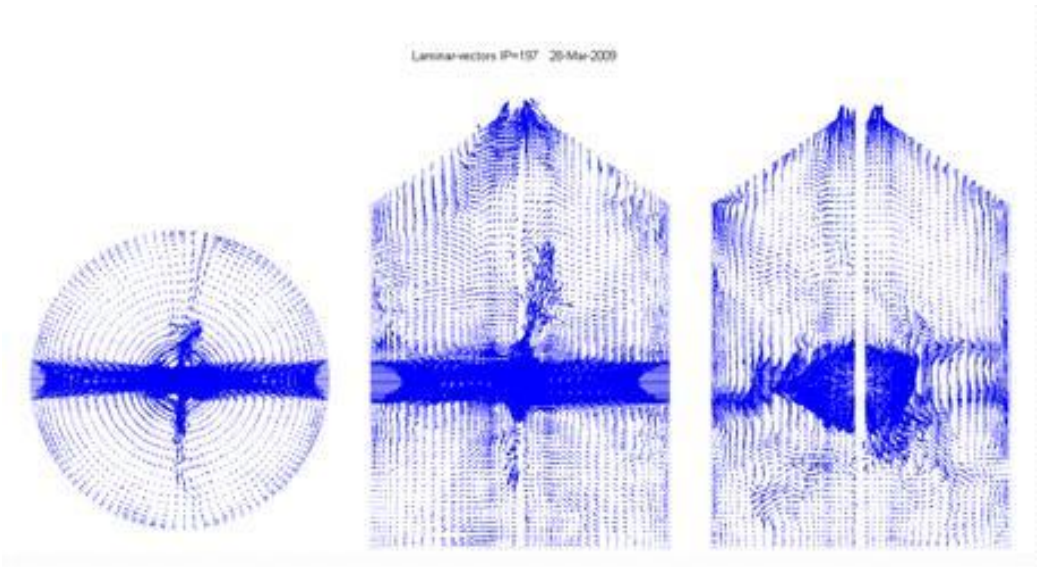

Fig. 7. (Link to Dynamics and Color in 'ppt' format). Dynamic views of the instantaneous velocity field as vectors. The inlet is with a laminar parabolic inlet.

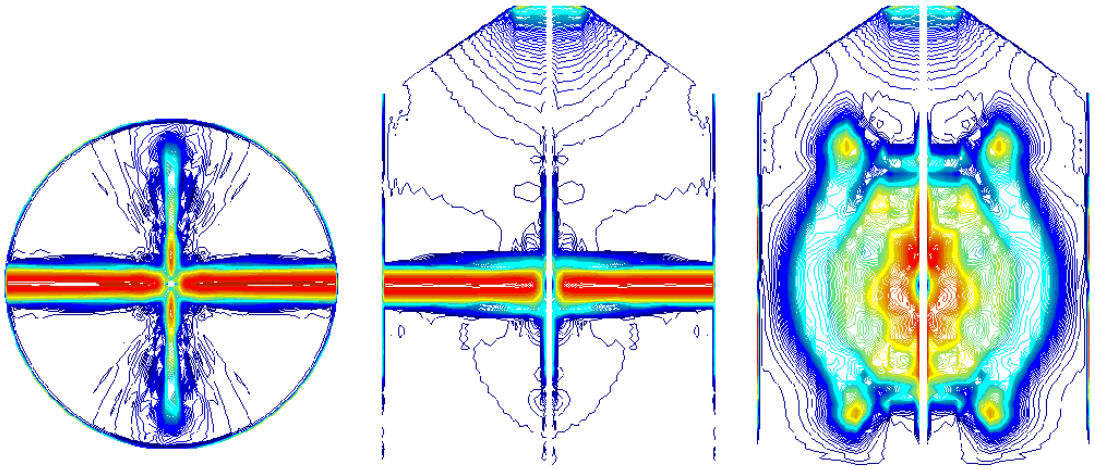

Fig. 8. (Link to Dynamics and Color in 'ppt' format). Three, centered, orthogonal dynamic views of the instantaneous velocity field as contours (100 contours). The inlet is with a laminar parabolic inlet.

visualize the laminar inlet flow. Since the contour plots offer a better (and prettier) picture, they are used here.

These dynamic figures show that the two coherent high-velocity jets and the resulting pancake flows are at a much higher velocity than the low velocity regions within the individual quadrants. When we questioned the inlet laminar conditions, we added another run using an average turbulent inlet without fluctuations. A plug case was also run as it would have the highest shear or velocity gradient at the edge of the jet. It would not be infinite as a result of the finite difference approximations used in the code. All the inlet cases are further discussed and the turbulent and plug flow cases are shown in the supplemental material online (SMO_05_Inlet Flow Conditions). Because they are dynamic visuals, they have to be further linked to OSU's Knowledge Bank. These additional dynamic views are contour plots like Fig. 8 and were generated with the same code with only the initial inlet boundary condition changed.

Figure 9 is a composite that shows the three center pictures for the three inlet conditions. This is the vertical jet view that best shows the development in time for the start-up part of the flow. The number of contour levels has been increased to 200 so as to show details better. The three views are synchronized in time and represent the first part of the flow that takes us into the fully turbulent

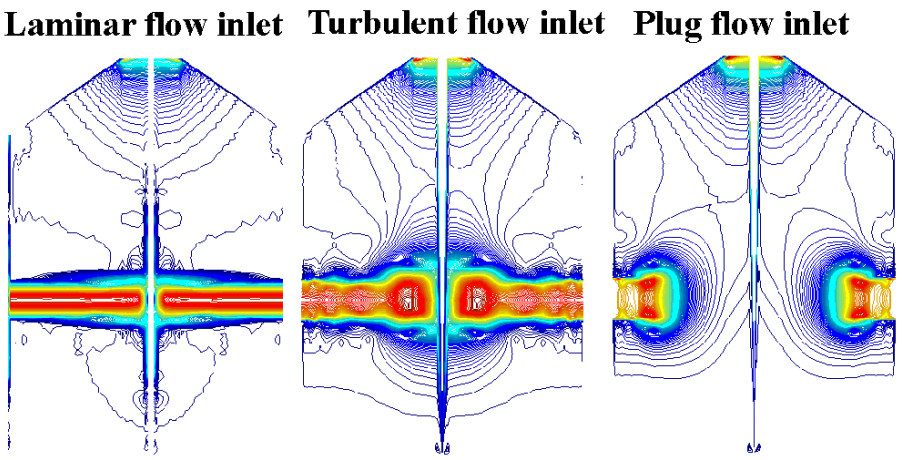

Fig. 9. (Link to Dynamics and Color in 'ppt' format). Dynamic vertical view between the jets for laminar, turbulent, and plug flow inlet conditions showing initial (start-up) segment (200 contours).

conditions. This is the largest image and can take up to 5 minutes to initially download. Once loaded on your local computer, it will replay quickly. Here, every 300th time step is shown with the start being at the 60th time step. What we thought would be a relatively minor change had a pronounced affect on the developing velocity field. This observation appears to be a result of the increased shear that exists near the boundary between the jet and the fluid in the vessel. The laminar inlet jet on the left is very different from the turbulent and plug inlet jets shown on the right. The laminar inlet is a clean jet in contrast to the right jet that clearly shows Rayleigh jet instability. The laminar initial conditions have the highest center-line velocity and the lowest shear rate at the edge of the jet.

The inlet jet diameter in the experiments was 1.27 cm and the tank radius was 4.45 cm. The jet diameter to tank radius ratio is only 3.5, which would represent the number of jet diameters from the inlet to the pancake region. The inlet average velocity was 15.45 cm/sec in all cases, which would translate to < 0.3 seconds for the fluid, on the average, to go from the inlet to the pancake. For the laminar inlet that would have a center line velocity of double this value, the time would be even less. For the laminar inlet case, the shear rate between the jet and the ambient fluid is not high enough and the transient time is not long enough for the Rayleigh instability to manifest itself. Whereas for the other two cases the instability can be clearly seen. For the turbulent case, the instability appears to start a fraction of a diameter from the nozzle. For the plug flow case, the instability appears at the nozzle exit. The mechanism of jet breakdown for the laminar inlet case is very different from the Rayleigh instability observed in the other two cases.

If one looks at the laminar inlet dynamic visual, one sees that from the start the two smooth jets enter from the sides, pancake in the middle, and spread outward towards the vessel walls. Since the exit is at the top, the downward directed part of the pancake is forced to circulate along the bottom and then return upward along the lower wall. When this return flow arrives back at the jet, it perturbs it. The disturbance is not balanced by the circulation pattern in the top half. The circulation will be less than in the bottom half because of the large exit flow. In the laminar case, the large scale circulation kicks off the jet instability while in the other two cases, the instability is internal to the jet (Rayleigh). Of course, the recirculation of fluid in the Rayleigh cases still exists and will also contribute to shortening the time needed to arrive at fully turbulent conditions. The turbulent inlet resulted in the shortest time. The laminar case rapidly evolved once it is started and beats out the plug flow case. The plug inlet flow, although not obtainable in actual experiments, covers a larger region in the beginning, but loses out to the laminar inlet case.

Although the start-up fluid dynamics is rich and interesting, it was to determine if the inlet conditions affect the fully turbulent conditions. Having answered this, we will stop with these visualizations and return to the main question, which is to establish what region of the flow to study and for how long must we average the data to obtain long-time averages.

3.3. Additional Comments on Preliminary Efforts

Since a start-up experiment is not available, Fig. 1 for the RMS was restricted to the fully developed turbulent region. The start-up is, however, available for the computations. The parallel to Fig. 1 for the computations includes the entire initial developing jets. Thus, the required averaging time will be longer. What should be done is to subtract out the initial part, which we estimate to be from 50 to 100 seconds. The plots and comments for the computational moments, which include the initial part, are available in the supplemental material online (SMO_07_Computational Averaging Time). For the fully developed turbulent region, we estimate that the average of the averages (1^{st} moment) levels out rapidly (~ 25 seconds) even though there is jet flapping of ~ 12 per second. The RMS requires more time. Here, an averaging time of 100 seconds should be adequate. Thus, unlike averages (1^{st} order), which can stabilize rapidly, the RMS (2^{nd} order) are all of the same sign and cannot do so as easily. The skewness and kurtosis require still more time as they involve the third and fourth order moments. Most of the skewness values are very close to zero so they matter little.

For the radial velocities, the values are negative for the long time averages and would indicate asymmetry toward more negative values. For these, the full 150 seconds or so are needed to level out. The curves for the kurtosis or flatness suggest that the distribution should be peaked as would be expected given that there are the jet velocities and the much lower surrounding velocity outside of the jets.

The effect of the inlet on the flow at fully turbulent conditions was compared for the laminar and turbulent inlet conditions. For the quadrant and central core regions, the inlet affect is small. Comparisons are available in the supplemental material online (SMO_08_Effect of Inlet Conditions at Pseudo-steady State Conditions).

In the time domain, for viewing, the selection of the frame rate is based on the researcher's judgment of what looks good; i.e., do you use all the stored frames or some fraction thereof. We settled on using every 3rd data set, which represents a slowdown factor of ~ 120. We wanted the flow to be clearly defined when the jets underwent larger scale motions (flapping) which resulted in rapid movements in the pancake region (~ 12 Hz). What one selects to view depends on the viewer. Some of our thoughts are given in SMO_09_Time Sequences of the Pseudo-Steady-State Flow Field.

Long time averages have long been used in the analysis of turbulence and can be important and valid statistical measures of the flow. However, in using such averages much of the richness of the fluid motions is lost. Yet, such measures have been and will continue to be important, especially when the design of a turbulent system is undertaken. A comparison of the instantaneous and long-time average results showed, once again, that the long time average does not look like the instantaneous pictures. The average is just what it is: an average representation over the period. For our numerical analysis of the fully turbulent region, the segment used represents ~ 235 seconds in real time. All the visuals are shown using three orthogonal views of the four statistical moments in the supplemental material online (SMO_10_Long Time Average Picture of the Flow).

For all of these, the high contour values are concentrated at the region at the edge of the jets and in the center interacting pancake region. These regions are, of course, where the two high speed jets first interact with the flow, pancake together, and change direction to move as a rapidly spreading disk of fluid towards the wall and then breakdown into a chaotic like turbulent flow. The importance of the pancake region is clear. This is the region where there are the most intense fluctuations. It is

also of note that the half jet spreading angle is close to 7.5 degrees as indicated by the converging cone of influence.

Average values are the highest in the jet flow field and are symmetric. The RMS is approximately an order of magnitude lower than the mean. The skewness is quite small and the kurtosis is somewhat larger. Results for other inlet conditions are similar. However, there are some small differences because the inlet conditions continue to influence the flow during the entire flow period.

Dynamic, 3-dimensional views for the initial region are also available, which cover the entire flow period (SMO_11_Three-Dimensional_View_of_the_Start-up_Flow). A great deal of effort went into making these visuals understandable. However, what one finds is still an overload of information in the 3-D pictures that makes it difficult to really extract anything worthwhile to say.

To summarize, the flow picture for the laminar input does not involve the Rayleigh instability. What appears to occur is the flow in the lower half becomes unsteady because of the wall interactions. When this higher speed unstable flow along the wall re-circulates back into the vicinity of the jet, there is a displacement of the jet that eventually results in the entire flow field rapidly breaking-down and becoming turbulent. For the turbulent 1/7 power-law inlet, the Rayleigh instability is clearly the mechanism. The 3-D dynamic graphic demonstrates that the small difference of the inlet conditions that are continuously imposed on the flow during the entire computation can have a major influence on the subsequent development of the flow field.

4. Sub-Volume Analysis

4.1. Details of the Sub-volumes used for Analysis

The sub-volumes used in our initial work were not critical as they were used to establish time requirements, spatial resolution, amount of data needed for a statistical average, etc. However, for detailed comparisons and understanding, we need to know the nature of the flow within the sub-volumes selected. Also, information involving the computation and experimental coordinate systems, grids used, and sub-volume definitions are all needed. The computational data are in polar coordinates and the experimental plots are in rectangular coordinates. The horizontal (x-y plane, constant z) cross-section of the experiments would be the same in both systems. There are sketches, tables, and explanatory figures available in the supplemental material online (SMO_13_Sub-Volume Analysis) to help with the details. The logical definitions of the sub-volumes selected (over 20) are

critical and key to being able to offer rational analysis, comparisons, and understanding of the results presented here.

4.2. Visual Views for Long-Time Averages for Individual Sub-volumes

The simplest way to visualize the flow is to look at a circular region in polar coordinates. In Fig. 10, the left view is for the long time average of the computations for the main part of the left jet with

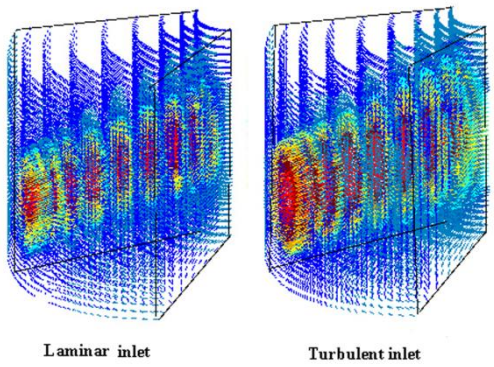

Fig.10. (Color online). Polar coordinate view of the left jet for both laminar and turbulent inlets (long time view).

the laminar input. For clarity, there are only 10 radial cuts shown. The right view is the same but for the turbulent inlet. The turbulent inlet condition gives a broader and flatter inlet. These are long time average views and the inlet conditions, which are boundary conditions, do not change during the computations.

Figure 11 shows two composite views. The left is for the jet region and the forward leg of the pancake. On the right is the view of the pancake. The laminar inlets and the exit are noted.

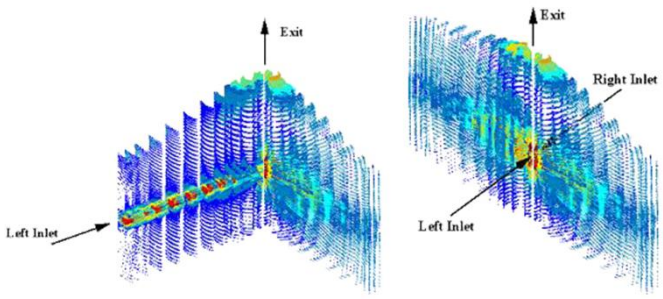

Fig. 11. (Color online). Composite views: left side is left inlet jet and forward pancake. Right side is the entire pancake.

The total number of entries in the sub-volumes ranged from ~ 9,000 to ~ 44,000 depending on the size of the sub-volume. These are long-time averaged computational results and should be adequate for averages. The jet velocity is radial in the entry region and is the highest velocity observed. This

is the primary flow. The RMS (2^{nd} moment) values in the jet are small (< 3% of the jet). As expected, the θ and z components of the jet velocity are even smaller (< 2% of the jet velocity). All the velocity components in the quadrants that are outside of the jet and pancake regions are small and are ~ 2% of the radial jet velocity. The pancake regions, which are the secondary flows, are ~ 11% of the radial jet velocity itself.

To look further into what histograms may provide, we eliminated null nodal points outside the sub-volume as they could introduce count errors. These ranged from 1.3 to 2% of the individual sub-volume counts. The histograms for the three components are in the supplemental material online (SMO_14_The velocity histograms for r, θ, and z components).

Skewness and Kurtosis values were separately measured. The skewness measures the degree of asymmetry of a distribution around its mean. Kurtosis values characterize the relative peakedness of a distribution compared with a normal distribution that has a value of 3. The average skewness of all regions and all components is - 2.5×10^{-5}. This value is small and negative and suggests there should be an asymmetric tail extending toward negative values. The Kurtosis values obtained (relative to 3) are small and positive; they suggest a distribution more peaked than would be expected for the Gaussian case. Finally, the z-velocities are positive since the outlet is at the top.

The qualitative aspects of our study were to look at the resulting vector and contour plots of the flow field from both the computational and experimental efforts and to compare them. The quantitative emphases are the statistical averages of the first four moments. These were determined, as well as possible, from the experimental data using about the same region of the flow field. This long-time average study can provide a measure of the overall ability of the code to reproduce the experimental results for the fully turbulent conditions.

5. Detailed Comparisons

5.1. Experimental and Computational Results in the Jet Regions

To undertake a detailed numerical comparison between results, we must be cognizant of what averaging volume should be used and of shortcomings in the data. The symmetric sub-volume used at the start to determine the length of averaging time was too large to allow detailed comparison to be made. There was too much being averaged. It would be like trying to work with an entire human population without regard to all the variations that exist within that population. Clearly we needed smaller volumes. To start, we selected the jet regions because we have a good idea of what they look

like. We used, for each side, the jet entry, jet center section, and the full jet. The only inputs to the CFD program are the inlet Reynolds number (2000) and the boundary conditions. All the conditions in tabular form are in the supplemental material online (SMO_15_Conditions for the Flow System).

Our first test was to validate the inlet velocities. To do this, we modified the sub-volume program to allow looking at the cross-flow plane right at the inlet and integrated across the plane to generate an average inlet velocity. The area of integration was a square shape that was a bit smaller than the actual flow area which was a circular shape. The integrated value was <14% high for the laminar inlet and <22% high for the turbulent case. The detailed visual comparison between the laminar and turbulent velocity distributions are as expected and are shown in the supplemental material online (SMO_16_Check of Inlet Velocity Distributions).

We need to comment further on the computational resolution grid as this affects directly our ability to compare results. As noted earlier, the computational results are sensitive to the total nodal density. Thus, an exact match is unlikely. One can hope that the higher resolution grid used here has brought us much closer to the reality of what is actually measured and that our comparisons will be adequate.

We will start by comparing the key numbers to illustrate the results (average velocity, standard deviation, and the ratio between them). For the experimental results, the difference in the left and right jets is < 17%. The experimental velocities along the jet are about 4 to 20 times the orthogonal values. For the CFD results, the difference in the left and right jets is ~ 7% and the ratio of the radial to theta components of the velocity is two orders of magnitude (20 to 36 times) and the radial to vertical ratio is even greater (38 to 55 times). The higher radial to vertical ratio can be attributed to the net upward flow as contrasted to no net flow for the angular direction. In our analysis, we used many bar graphs to make comparisons that are in the supplemental material online. For example, one of these (SMO_17_ Details of the Jet Region, Average Velocities, Laminar Inlet) is for the 6 jet sub-volume regions under laminar inlet conditions for the experiments, computations, and their ratio. The similarity between each of the 6 jet sub-volumes is very apparent. There are, however, small differences observed. We can speculate the cause of the differences: a) the lack of high enough grid resolution in the computations, b) not knowing the parameters well enough for normalization used in the computations, c) the experimental inlet profiles being more turbulent or transitional rather than

laminar, d) not being able to measure very low velocities (~ 1 cm/s) in the experiments with high success rates, e) or a combination of all of these?

The ratios of the computations to the experiments are the crux of the matter for this work. That is, how well do the computations check with the experiments? For the radial velocities the ratio is 1.65 ± 0.18 or 10.7%. This is good when one realizes there are no adjustable parameters involved. On the average, the radial velocity ratio difference is between factors of 1.4 to 1.9. The other components of the velocity are nearly two orders of magnitude lower than the jet velocity; thus, any percentages reported here are based on the jet velocity rather than the actual velocity. For these, the *y* or *o* component ratio is 0.46 ± 0.33 and the *z* ratio is 0.27 ± 0.06. The radial velocities in the computations are greater than the experimental, while the other components are less. All in all, the computations and experiments are in good accord.

5.2. Influence of Inlet boundary Conditions on the Jet Regions

Similar results were obtained for the turbulent inlet conditions ($1/7^{th}$ power law) and are available (SMO 18 Details of the Jet Region, Average Velocities, Turbulent Inlet). The average inlet velocities are the same; however, the laminar profile will have a higher center-line velocity than the turbulent one. The inlet velocity might affect the long-time-average results, since it is applied as a boundary condition that does not change with time. The average velocity for the turbulent inlet is 9.61 cm/sec ± 0.43 and for the laminar, 8.57 cm/sec ± 0.69. For the comparison of the computations to the experiments, the ratios range from ~ 0.61 to ~ 0.55 with the standard deviation changing from ~ 10.6% to ~ 14%.

With this degree of similarity between the two inlets, we conclude that the long-time-averages in the pseudo-steady-state turbulent regime are nearly independent of the initial conditions. What we see here is two flows with two very different initial conditions develop from start-up to the fully turbulent by very different paths and on the average arrive at very nearly the same place. This is, of course, exactly what we believed would be true for turbulence and are gratified that our work shows this.

5.3. Some Additional Comments about the Flow

Parallel bar-graph comparisons for the *quadrants* can also be found (SMO 19 Details of the Quadrant Regions). The briefest of the ideas are given here. Each quadrant contains half a jet, half of the pancake region, and a quarter of the low velocity region. Thus, average velocities are much lower,

by a factor of four, than those experienced in the jets. However, the plots look quite similar when one takes into account that the scale is reduced.

The *pancake* region is a bit different in that we have not used the absolute values (SMO_20_Details of the Pancake Regions). So as to concentrate on the velocity magnitudes, we have also eliminated the ratios in this figure. We expect the pancake velocities to lie between the high values in the jets and the low overall average in the quadrants and this is what is observed. For the jet the average velocity is 0 - 10 cm/sec; for the quadrants, 0 - 2.5 cm/sec; and for the pancake regions 0 - ±5 cm/sec, which is nicely in the middle as expected and observed. The vertical CFD velocities, above the jets are positive and below are negative, as expected. The experimental vertical velocities below the jets are still negative, but reduced from those observed above the jets.

The Reynolds number was changed to that of the tank (571.4 versus 2000) and the CFD run repeated. Since the Reynolds number is used to normalize the computational results, there was little difference in the output computational values (< 0.7% for the radial velocities in the jet region). Of course, the reference velocity will be considerably different, which reflects in a large change in the actual velocity in cm/s. These results demonstrated that using the inlet Reynolds number is the proper choice.

A more detailed study of the higher order moments (skewness and kurtosis) has led us to question the accuracy of these values for the experimental data. We cannot fairly judge the standard deviation, but, it looks quite reasonable. We believe the problem is associated with the experimental resolution. To get to the moment calculations, the randomly measured vectors must first be placed on the experimental grid (< 10,000). Then, after this, results using any products or derivatives will have even further reduced accuracy. These nodal values are subsequently averaged again over the specific sub-volumes being considered. In spite of this uncertainty, all the moments (both CFD and experiments) were plotted for the front left quadrant (SV #15). We then thought that the left half jet sub-volume (SV #1) might be a better sub-volume to use because of higher velocities. All of these results are available at SMO_21_Higher Order Moments. Note that the general trends for the CFD results are the same for all the moments. The only explanation we have for the lack of agreement for the experiments is that the errors are large in the post-processing of the velocity vector data because of extrapolation to the experimental nodal points and the need to use higher powers for the higher moments.

We also wondered if we could track the experimental results in time and compare them with the computations. This does not seem possible at the present for a variety of reasons. The major problem was trying to set the initial fully 3-D, instantaneous, velocity-vector conditions on the computational grid from the sparse experimental grid so that step by step short term computations could be made. Many attempts were made, but every effort failed as a result of not being able to satisfy continuity at the beginning of the computations. If this could be done, one might be able to answer some very interesting questions such as is the system so chaotic that from "identical" initial conditions for the experiments and computations, the results could be very different? One might ask how different are they? In truly chaotic systems, small differences can lead to rapidly divergent results in time. This does not mean there is anything wrong with either, but that the system can be so chaotic that tracking in time is useless. The two are simply different realizations of the flow field and there is nothing to be gained by comparisons in the time domain.

6. Summary

In many ways this paper is already a summary of many years of work. Here we want to concentrate on a few highlights.

For the experiments: a) our unique particle tracking (PTV) experiments, when compared to the computations, are of low resolution (1:100). However, they are unique and cost effective. One can obtain time resolved, velocity vector information in all of the space. b) Our system has a minimum velocity limit. Also, the higher moments (3^{rd} & 4^{th}) from our experiments do not appear to be accurate. c) For averaging in time, each experimental frame does not have enough vectors to give a smooth picture of the flow; thus, a number of frames have to be averaged.

For the computations: a) jet flapping requires long averaging times. b) Results using different inlet conditions show that pseudo steady-state turbulence is independent of initial conditions. c) High values of the higher moments are along the edge of the jets and in the center interacting pancake region. d) The jet velocity is the primary flow. The pancake regions are secondary flow (~ ½). The quadrants are the lowest (~ 1/5) because of counteracting velocities in all directions and very low velocities away from the jets and pancake regions.

For comparison of CFD and experiments: a) The r - component CFD/Exp ratio is 1.65 ± 0.18 or 10.7%. The range is 1.4 to 1.9. The CFD and experiments are in good accord since there are no adjustable constants. b) The ratios for other components are generally lower by a factor of 1/4 to 1/2.

c) To compare experiments with CFD results in time we need to have a fully 3-D initial condition from the experiments. This initial picture must satisfy continuity as close as possible. d) The resolution difference makes interpolation difficult. Our attempts so far have failed. Attempts to impose continuity have also failed.

7. Acknowledgements

There are many early coworkers and students that have contributed to this work. A few of them must be specifically mentioned: Yann Guezennec and his students were instrumental in the development of the particle tracking technology. Jim Wallace and Helmut Eckelmann were colleagues in the development of the quadrant splitting and pattern recognition techniques to study coherent structures. Fernando Muzzio and Bob Brodkey obtained a joint NSF grant to use the opposed jet geometry to try to fully rationalize turbulent flow in that system. This was directly the basis, so many years ago, for the present work reported here. The graduate and undergraduate students and faculty listed as authors are only the top of the pyramid.

It is still to the future researchers to provide us with the *'why?'* all of this happens. We feel strongly that this lies in the dynamics of the space and time development of turbulent structures. What we observe at any instant of time is an average of what we call flow development. There are new, middle aged, and old structures of all different sizes that are mixed together and presented to us as a composite picture. Our technique of pattern recognition allows us to extract some predominant characteristics depending upon the criteria we set, but this is a superimposed picture of many steps through time. None of this really gives us the dynamics; i.e., how does one structure develop into the next. What we need next is to make quantitative what is often a mechanistic cartoon of the time evolution of specific turbulent elements. Currently, this lies in the heads of the researchers and is in need of further verification.

8. References

Choi W-C, Guezennec, YG (1997) In situ calibration for wide-angle, three-dimensional stereoscopic image analysis. Applied Optics, 36: 7364-7372.

Choi W-C, Guezennec, YG (1998) Measurement of cycle-to-cycle variations and cycle-resolved turbulence in and IC engine using a 3-D particle tracking velocimetry. JSME International Journal, 41: 991-1003.

Guezennec YG, Brodkey RS, Trigui N, Kent, JC (1994) Algorithms for fully automated three-dimensional particle tracking velocimetry. Exps. in Fluids 17: 209-219.

Kent JC, Trigui N, Choi, W-C, Guezennec YG, Brodkey RS (1993) Photogrammetric Calibration for Improved Three-Dimensional Particle Tracking Velocimetry (3-D PTV). Proc. SPIE, 2005: 400- 412.

Nakamura S (1997) Options and selection of numerical algorithms for unsteady incompressible Navier-Stokes equations. ASME FEDSM97-3666.

Nakamura S, Brodkey RS (1999) Computational and experimental study of the fluid flow in a cylindrical cavity with an impeller rotator at an eccentric location. ASME/JSME Joint Fluids Engineering Conference, July 18-23, 1999, San Francisco, CA, FEDSM99-7193.

Nakamura S, Brodkey RS (2000a) Direct and large eddy simulation of the three-dimensional unsteady flows in the counter-jet mixing vessel. ASME Fluids Engineering Summer Conference, June 11-15, 2000, Boston, MA, FEDSM2000-11007.

Nakamura S, and Brodkey RS (2000b) Computational flow analysis for the chemical mixing vessel with impeller and baffles. ASME Fluids Engineering Summer Conference, June 11-15, 2000, Boston, MA, FEDSM2000-11207.

Rhie CM, Chow WL (1982) A numerical study of the turbulent flow past an isolated airfoil with trailing edge separation. AIAA/ASMIE 3rd Joint Thermophysics, Fluid, Plasma and Heat Transfer Conference, AIAA-82-0998.

Trigui N, Guezennec YG, Kent JC, Brodkey RS (1992) Fully automated three-dimensional particle image velocimetry system applied to engine fluid mechanics research. Proceedings of Int. Seminar on Optical Methods and Data Processing in Heat and Fluid Flow, London, April 2-3.

Unger DR, Muzzio FJ, Brodkey RS (1998) Experimental and Numerical Characterization of Viscous Flow and Mixing in an Impinging Jet Contactor. Can. J. Chem. Engr., 76: 546-555.

Zhao Y, Brodkey RS (1998a) Averaged and Time-Resolved, Full-Field (Three-Dimensional), Measurements of Unsteady Opposed Jets. Can. J. Chem. Engr., 76: 536-545.

Zhao Y, Brodkey RS (1998b) Particle Paths in Three-Dimensional Flow Fields as a Means of Study: Opposing Jet Mixing System. Powder Technology 100/2-3: 161-165.

Zhao Y, Brodkey RS, Nakamura S (2001) Study of 3-D Mixing Processes by Numerical and Experimental Approaches. ASME Fluids Engineering Summer Conf., June 11-15, 2001, Boston, MA, FEDSM2001-11007.

Zhao Y, Brodkey RS, Nakamura S (2002) Study of 3-D Mixing Processes by Numerical and Experimental Approaches. ASME Fluids Engineering Division Summer Meeting, July 14-18, 2002, Montreal, Quebec, Canada, FEDSM2002-311697.